Engineering an ultra-fine grained microstructure, twins and stacking faults in PBF-LB/M Al-Si alloy via KoBo extrusion method

P Snopiński, K Matus, M Łagoda, A N S Appiah, J Hajnyš

Engineering an ultra-fine grained microstructure, twins and stacking faults in PBF-LB/M Al-Si alloy via KoBo extrusion method

P. Snopiński[1], K. Matus[2], M. Łagoda[3], A. N. S. Appiah[2], J. Hajnyš[4]

[1]Department of Engineering Materials and Biomaterials, Silesian University of Technology, 18A Konarskiego Street, 44-100 Gliwice, Poland;

[2]Materials Research Laboratory, Faculty of Mechanical Engineering, Silesian University of Technology, Konarskiego 18a St, Gliwice, 44-100, Poland

[3]Łukasiewicz Research Network - Institute of Non-Ferrous Metals, Sowińskiego St. 5, 44-100, Gliwice, Poland

[4]Faculty of Mechanical Engineering, VSB-TU Ostrava, 17. Listopadu 2172/15, 708 00 Ostrava, Czech Republic

*corresponding author e-mail: przemyslaw.snopinski@polsl.pl

Abstract

In this study, the microstructural and mechanical properties of an PBF-LB/M AlSi10Mg alloy extruded by the KoBo process are investigated. Electron backscatter diffraction (EBSD) and transmission electron microscopy (TEM) analyses revealed an ultrafine-grained face-centred cubic (f.c.c.) matrix with a high density of stacking faults (SFs) and Σ-CSL twin boundaries (TBs). The KoBo processed sample exhibited an attractive combination of mechanical properties - moderate tensile strength of 324 MPa and excellent ductility - elongation at break of ~10%. The unique alloy microstructure obtained has the potential to exhibit superior properties such as improved radiation resistance, high temperature stability, resistance to intergranular corrosion and cyclic deformation. Overall, the results of this study provide a simple way to tailor the strength and ductility of PBF-LB/M-Al-Si alloys through grain boundary engineering and manipulation of TBs and SFs through interface engineering.

Keywords

Laser-based powder bed fusion of metal (PBF-LB/M); AlSi10Mg alloy; KoBo extrusion process; Ultrafine-grained microstructure; Transmission electron microscopy (TEM)

Introduction

The term "nanotwinned" (NT) refers to a type of metallic material that contains a high density of nanoscale twin boundaries. NT materials are characterised by exceptional strength and ductility, excellent thermal stability [1], good electrical conductivity [2], and improved tolerance to radiation damage [3] [4], making them ideal materials for applications in the electronics, nuclear, and aerospace industries. To date, most recent studies have focused on low stacking fault energy (SFE) materials such as Cu (SFE_{Cu}= 22 mJ/m^2) [5] [6], Ag (SFE_{Ag}= 16 mJ/m^2) [7] [8], stainless steel (SFE_{Fe}= ~50 mJ/m^2) [9] [10][11] and some high entropy alloys [12] [13], where it is much easier to introduce twin boundaries (TBs). Lu et al. [14] found that NT copper has a very high strength (900 MPa) with high ductility (7.5%). This is due to the fact that TBs act as barriers to mobile dislocations in a similar way to grain boundaries, resulting in a strengthening. Other researchers [15] have shown that NT copper thin films have a high strength to electrical conductivity ratio. They found that stacking faults/nanotwins contribute to electron scattering, resulting in increased electrical conductivity. Moreover, numerous in situ ion irradiation studies [16] [17] [18] and molecular dynamics simulation works [19][20] visualized direct interaction between irradiation-produced defects and TBs. Phase and twin boundaries can transport and eliminate radiation-induced defects, thus alleviating irradiation damage [21]. In addition, stacking faults, coherent twin boundaries (CTBs) and Σ3 (112) incoherent twin boundaries (ITBs) have been shown to play a crucial role in the deformation process of these low-SFE NT metals [22].

Although significant efforts have been made in studying the NT low SFE metals, little attention has been paid to the metals with high SFE such as aluminium alloys (SFE_{Al}= 120–165 mJ/m^2). This is because high SFE provides a lower propensity for twin formation. Therefore, these metals have to be usually alloyed with other elements to lower their SFE and promote the formation of growth twins. In recent years, by surface engineering [23] [24] [25], deformation at cryogenic temperature [26] or by using reinforcements (CNTs/SiC) [27] [28], researchers have successfully fabricated NT aluminium alloys. For example, via magneton sputtering, Richter et al. [24], synthesized Al-Zr alloy films containing an abundance of incoherent twin boundaries and 9R phases, exhibiting hardness of 4.2 GPa. Using DFT calculations they revealed that the addition of Zr reduces the SFE of the Al alloy, thus allowing incoherent TBs formation. Gong et al. [29] manufactured NT composite through the addition of SiC to the aluminium matrix using the pressure infiltration method and found that SiC/Al composites with SFs (stacking faults) reached proportional limit (σ_{p5} and σ_{p100}) of 65 MPa and 124 MPa, respectively. They related SFs formation to the lattice distortion fluctuation in Al matrix (fluctuation of effective SFE) and the SFs origins from decomposition of full dislocations. Liao et al. [30] fabricated nanocrystalline (NC) aluminium through the cryogenic ball milling process. They discovered that wide SFs are formed due to the NC structure and possibly also to the interaction of SF ribbons with high density of dislocations. Furthermore, bulk NT metals have also been successfully fabricated using high-strain severe plastic deformation methods (SPD) such as Equal-Channel Angular Pressing (ECAP), High-pressure torsion (HPT) or Accumulative roll bonding (ARB) [31] [32] [33] [34] [35] [36] [37]. What's more the NT microstructure can be generated by dynamic plastic deformation (DPD) [38].

Quite recently, the effect of KoBo extrusion process on the grain boundary character evolutions in 1xxx series aluminium alloys was investigated. The distinctive characteristic of the KoBo method lies in its high-frequency, cyclic alteration of the deformation route. This process is well-known for inducing a substantial accumulation of point defects at the atomic level, such as vacancies and self-interstitial atoms (SIAs), which can alter the material's physical (thermodynamic) state [39]. This phenomenon, in turn, facilitates the formation of nanotwins, as the accumulation of SIAs is a precursor to nanotwinning [40].

While extensive research has been conducted on PBF-LB/M AlSi10Mg alloys, with a particular emphasis on surface engineering [41] [42] [43], post-fabrication heat treatments [44] [45] [46], and severe plastic deformation [47], studies addressing grain boundary character control are relatively scarce. To the best of our knowledge, there are is only one relevant research documenting the change of grain boundary character in PBF-LB/M AlSi10Mg alloys subjected to friction stir processing [48].

Therefore, in this investigation, we explore the application of the KoBo process, exposing PBF-LB/M-Al alloys to the extreme conditions of high strain and strain rate. The goal of this research is to increase the fraction of low-Σ coincidence site lattice (CSL) boundaries ($1 \leq \Sigma \leq 29$) and interrupt random boundary network connectivity through KoBo-processing for optimizing grain boundary character distribution (GBCD) and accordingly to modify properties of the PBF-LB/M AlSi10Mg alloy. The novelty of this work lies in the comprehensive analysis of an PBF-LB/M AlSi10Mg alloy subjected to the KoBo extrusion process, with a focus on both microstructural and mechanical properties. Through in-depth analyses utilizing Electron backscatter diffraction (EBSD) and transmission electron microscopy (TEM), our investigation unveiled an ultrafine-grained face-centered cubic (f.c.c.) matrix characterized by a notable abundance of stacking faults (SFs) and Σ-CSL twin boundaries (TBs). The outcomes of this research offer a straightforward approach to customize the strength and ductility of PBF-LB/M-Al-Si alloys by employing grain boundary engineering.

Experimental procedure

The AlSi10Mg alloy specimen with a diameter of 60 mm and a height of 60 mm was fabricated by the selective laser melting (SLM) method using spherical gas-atomized powder. Information about the powder's chemical composition can be found in Table 1. The SLM process parameters crucial for the production of compact specimens are listed in Table 2.

Table 1. Chemical composition of the AlSi10Mg powder used in the 3D printing process, in wt.%.

Al	Mg	Si	Ti	Cu	Fe
87.8	0.5	10.5	0.15	0.15	0.09

Table 2. Selective laser melting process parameters.

Laser power, W	175
Layer thickness, mm	0.02
Laser scanning velocity, m/s	1.4
Scanning strategy	Meander with 67° rotation

The PBF-LB/M sample was post-processed via KoBo extrusion method, of which the principal description can be found in Ref. [52]. The punch speed was 0.2 mm/s, the frequency of die oscillations was 5 Hz, and the oscillation angle was ±8°. The extrusion was carried out in one step with the extrusion ratio λ = 225 (Ø60 → Ø4). The true strain was calculated as ε_r=5.42.

Cross sections of the as-built and KoBo deformed specimens were examined by scanning electron microscopy (SEM). EBSD (electron backscatter diffraction) analyses were performed using a ZEISS Supra 35 scanning electron microscope operating at an accelerating voltage of 20 kV, a working distance of 17 mm and a tilt angle of 72°, using step sizes of 0.2 µm (as-built) and 0.06 µm (KoBo). Samples for microstructural analyses were prepared conventionally - mechanically ground with SiC papers, polished with diamond pastes and finely polished with 0.04 µm colloidal silica. Brandon's criterion was used for coincidence site lattice (CSL) boundary classification.

Thin lamella samples for the S/TEM study were cut in a cross section parallel to the ED plane in the ND-TD plane by focused ion beam milling (FIB). The microstructures of the thin lamellae and phase identification were studied using an S/TEM Titan 80/300 transmission electron microscope (TEM), at an accelerating voltage of 300 kV. The microstructures were characterized in bright field mode (BF), dark field mode (DF) and high-resolution transmission (HRTEM) mode. The obtained electron diffraction images were further analysed using Digital Micrograph and CrysTBox software.

All tensile tests were performed on a Zwick Z100 servohydraulic materials testing machine (capacity 100 kN) at a test speed of 1.0×10^{-3} s^{-1} at room temperature. The specimens were loaded along the build direction (as-built condition) and the extrusion direction (KoBo condition).

Results

Figures 1(a) and (b) show the result of the microstructural analysis performed in the scanning electron microscope. For the "as-built" initial state sample, chemical etching reveals the melt pool structure consisting of three distinct zones: the coarse melt pool zone (MP coarse), the heat affected zone (HAZ), and the fine melt pool zone (MP fine); whereas, for the "KoBo" sample, a homogeneous microstructure with numerous dot-like Si precipitates ranging from 0.1 µm to 0.3 µm in size.

Figs. 1(c) and (d) show the grain boundary maps superimposed on the inverse pole figure maps in the z-direction (IPF-Z). These images reveal that the initial state of the sample displays a coarse-grained structure with a relatively random texture. In contrast, the "KoBo" sample exhibits a submicrometric microstructure in which the majority of the grains are oriented along the <111> and <001> directions, a typical characteristic for extruded alloys [53]. It's worth noting that grains oriented in the <001> direction are less common but are considered recrystallization derivatives [54]. The supplementary data in Fig. S1 indicates that the coarse grains of the PBF-LB/M AlSi10Mg alloy were refined through the dynamic recrystallization process (DRX), resulting in a reduction of grain size from approximately 2.6 µm to about 0.8 µm. Referring to the statistical data given in Table 3, LAGBs and HAGBs account for 22.2% and 77.8% in the as-built sample and 9.4% and 90.6% in the KoBo sample, respectively. Furthermore, a significant number of high-angle boundaries fall within the range of 48-60° (Fig.

S2), which is within the spectrum typically found in FCC aluminum with CSL m3m symmetry space group boundaries [55]. It is also evident from Fig. S3 that the KoBo extrusion significantly modifies the fraction of the CSL boundaries (Σ3, Σ5, Σ11, Σ13b, and Σ25b). The largest change in the volume fraction of CSL boundaries concerns Σ11, Σ13b (both are twin boundaries) [56], and Σ25b (nucleus of primary recrystallization) [57], whose fractions increased by 5, 4.5, and 6.8%, respectively. These increases in the fractions of CSL boundaries may be attributed to atomic interactions related to grain boundary migration during dynamic recrystallization (DRX) [58] [59].

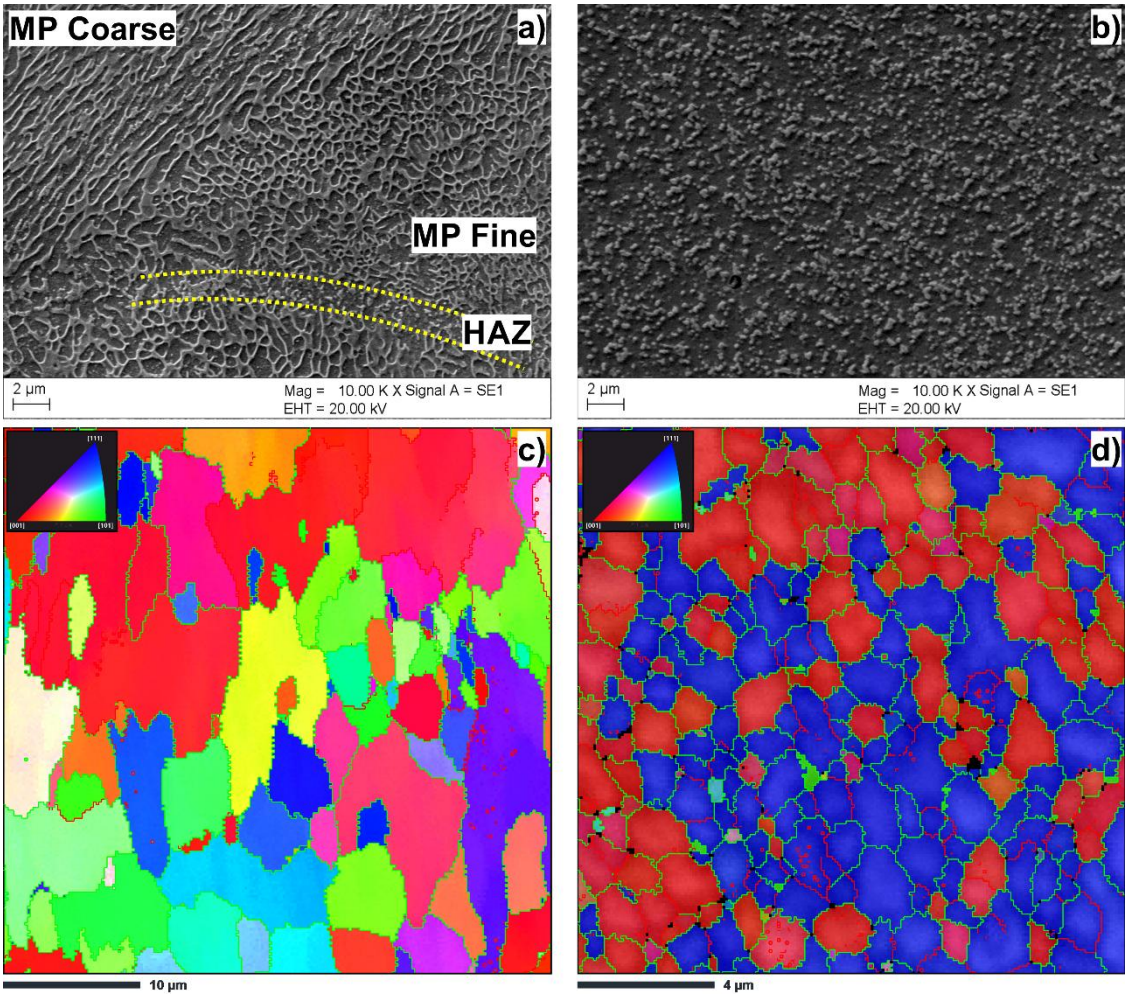

Figure 1. Microstructure of the as-built and KoBo samples a) SEM image of as-built sample taken on the X-Y (built) plane, b) SEM image of KoBo sample taken on the ND-TD (extrusion) plane, c) IPF-Z image taken on the ND-TD (extrusion) plane of as-built sample, d) IPF-Z image taken on the ND-TD (extrusion) plane of KoBo sample (note that the red lines in the IPF images correspond to the low angle grain boundaries, green lines to the high angle grain boundaries, while black points to the unidentified areas).

Table 3. LAGB (2° ≤ ϑ ≤ 15°), HAGB (ϑ ≥ 15°) fraction (%) and grain sizes for as-built and KoBo samples.

	As-built	KoBo
LAGB, %	22.2	9.4
HAGB, %	77.8	90.6
Grain size, µm	2.64 (GTA = 2º)	0.81 (GTA = 2º)

TEM observations were then carried out to examine the microstructures in more detail. Figures 2(a) and (b) depict bright and dark field TEM images along the X-Z plane (building plane). They show that the high solidification rate promotes columnar epitaxial grains [60] and that the unique feature of PBF-LB/M alloys is the intricate network of dislocations that forms as a result of the rapid solidification rate. Figure 2(c) presents the HRTEM image taken near the Al/Si interface and

the corresponding FFTs (insets). It reveals crystalline Al and amorphous Si phases. The presence of amorphous Si can be attributed to the short existing melt pool (rapid cooling enables transformation of the crystalline silicon phase into the amorphous state) [61].

The bright- and dark- field TEM images (Figs. 2(d) and (e)) confirm the strong grain refinement after KoBo extrusion and show a practically dislocation-free structure. It can also be seen that the equiaxed subgrains exhibit relatively strong contrast and sharp boundaries. In addition, an image taken in HRTEM mode shows many stacking defects (which were also observed in ECAP-processed samples [62]), spherical precipitates, and nanodimensional defects, the latter typically observed in KoBo-processed materials [39].

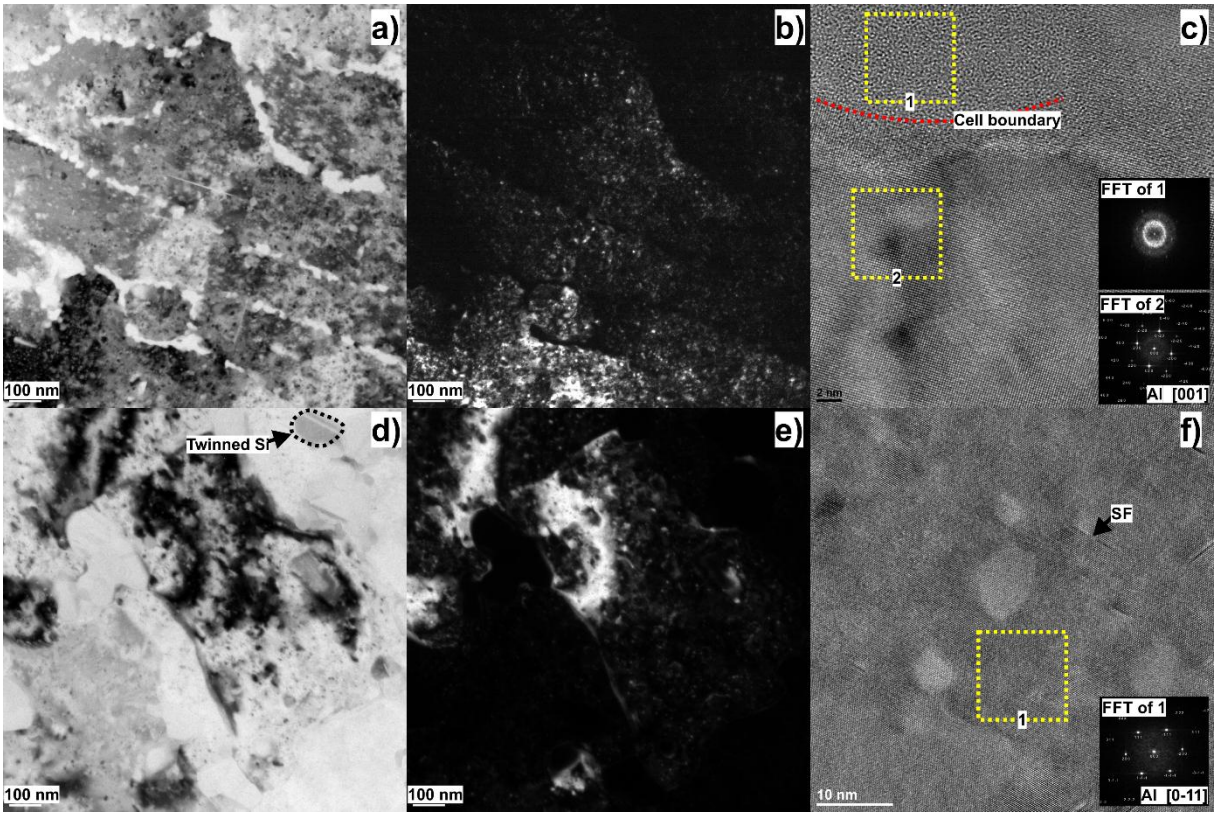

Figure 2. Representative TEM images of as-built sample (a) Bright-field TEM, (b) dark-field TEM images, (c) HRTEM image, and KoBo sample (d) Bright-field TEM, (e) dark-field TEM images, (f) HRTEM image taken from the grain vicinity, revealing multiple stacking fault defects.

Figures 3(a) and (b) show the bright- and dark-field TEM images with a round, 150 nm wide Si precipitate in the centre. In this image, microregions analysed with HRTEM are indicated by the square dotted lines. Figure 3(c) represents the Al grain boundary region indicated in Fig. 3(a). As can be seen, the HRTEM image unveils a twin boundary with a measured misorientation of 142.92 °. This value deviates from the theoretically expected misorientation of 141 ° or 144 ° for a twin boundary. However, this small deviation is below the maximum allowed deviation from coincidence according to the Brandon criterion (5 ° for the twin boundary) [63]. According to Wang et al. [64] such a GB with a kink angle of 141 ° appears when the twin is formed by 90° partial dislocations.

Upon closer examination of the phase interface depicted in Figure 3(d), it becomes apparent that there are segments featuring incoherent twin boundaries (ITBs), which is illustrated in greater detail in Figure 3(e). The Fast Fourier Transform (FFT) pattern (No. 2) confirms the presence of a structure with a high density of ITBs. This specific structure is typically categorised as a 9R phase, resembling structures previously observed in metals with a low stacking fault energy (SFE) [65]. While Figure 3(e) does indicate the presence of ITBs, suggesting the existence of at least some volume of 9R phase, but the precise measurement of the volume of 9R phase in the analyzed alloy is beyond the scope of this study.

Moreover, it is crucial to take into account the potential influence of a meandering boundary aligned parallel to the film plane, which could contribute to this observation in high-resolution transmission electron microscopy (HRTEM) mode [66]. It should also be mentioned that the existence of the 9R phase in the investigated PBF-LB/M Al-Si alloy is quite surprising, since its formation energy is much higher than that of nanotwins and it is highly unstable in high SFE alloys. However, the formation of the 9R phase has been confirmed in Al films deposited on a Cu substrate [31], nanostructured Al/AlN multilayer films [67], and Al-Mg alloys [68], among others.

Another interesting microstructural feature seen in Figure 3(e) is the presence of an amorphous region within the Si precipitate that resembles a deformation twin. The Fast Fourier transform (FFT) of the corresponding region (No. 4 in Fig. 3(e)) shows a diffuse halo ring, providing confirmation of the existence of an amorphous phase. It is plausible that this amorphous region formed due to increased phase stresses caused by the load-transfer effect between the soft Al and hard Si phases during plastic deformation [69]. It has been suggested that the formation of the a-Si phase may be due to a shear-driven amorphization process that transitions from the dc-Si phase to the dh-Si phase (dh hexagonal (dh) Si, Si IV (A), or 2H Si) when the shear stress exceeds 6 GPa [70].

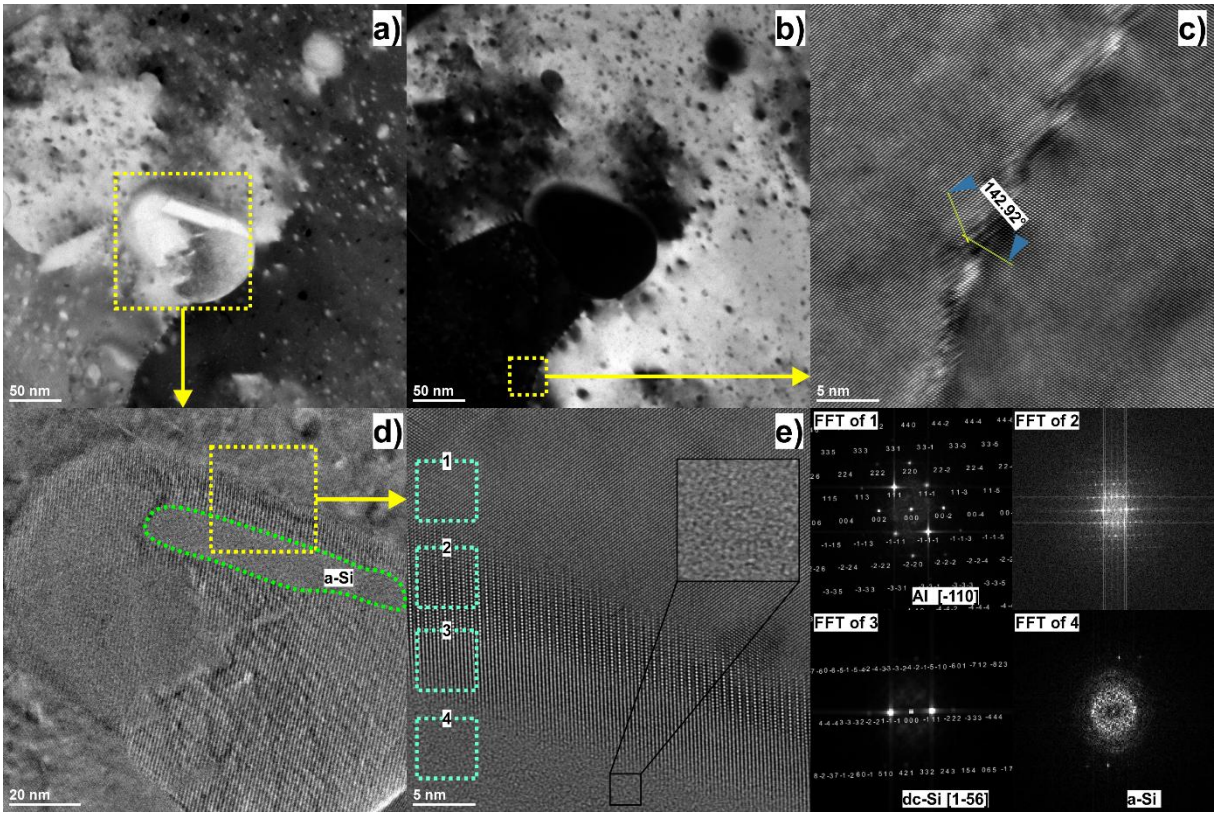

Figure 3. Representative TEM images of KoBo specimen a) bright-field TEM image, b) dark-field TEM image – Both micrographs reveal a Si precipitate locate in the centre and grain boundary area. Note that in the vicinity of grains multiple dot-like defects exists. C) HRTEM image of the boundary area highlighted in (b), d) HRTEM image of the Si precipitate, e) HRTEM image of the heterophase boundary area highlighted in (d) (the ITB has wide stacking faults inside).

Figures 4(a) and (b) present bright- and dark-field TEM images captured in another area, featuring a distinct Si precipitate and a well-defined grain boundary (highlighted by red arrows). The corresponding selected area electron diffraction (SAED) confirms that the Si precipitate, measuring approximately 300 nm, exhibits a twinned microstructure (Fig. 4(c)). Furthermore, an HRTEM image of the interface region, indicated by the dashed yellow square in Figure 4(a), reveals the presence of an amorphous band (a-Si) spanning approximately 20 nm within the precipitate (Fig. 4(d)).

Figure 4(e) shows a typical high-resolution transmission electron microscopy (HRTEM) image, revealing the atomic structure of the symmetric tilt grain boundaries (STGBs) with a Σ=3/(111)/109.47° orientation relationship. The presence of

Σ3 (111) grain boundaries observed through HRTEM aligns with the Electron Backscatter Diffraction (EBSD) data. Supplementary Figure S2 illustrates that the Σ3 grain boundaries account for about 4% of the CSL GBs. The grain boundary simulation in Figure 4(f) provides a clear view of the excellent atomic fit between both grains. However, upon closer inspection, Figure 4(g)), it becomes apparent that the STGB is interconnected by incoherent segments. In addition, stacking faults are found near the Σ=3/(111) STGBs. The STGBs could be formed by the mechanism described in the following study [71] which involves splitting and subsequent migration of a GB segment leaving two coherent twin boundaries [71], while SFs could be formed by the nucleation of double-Shockley particles from GBs [72].

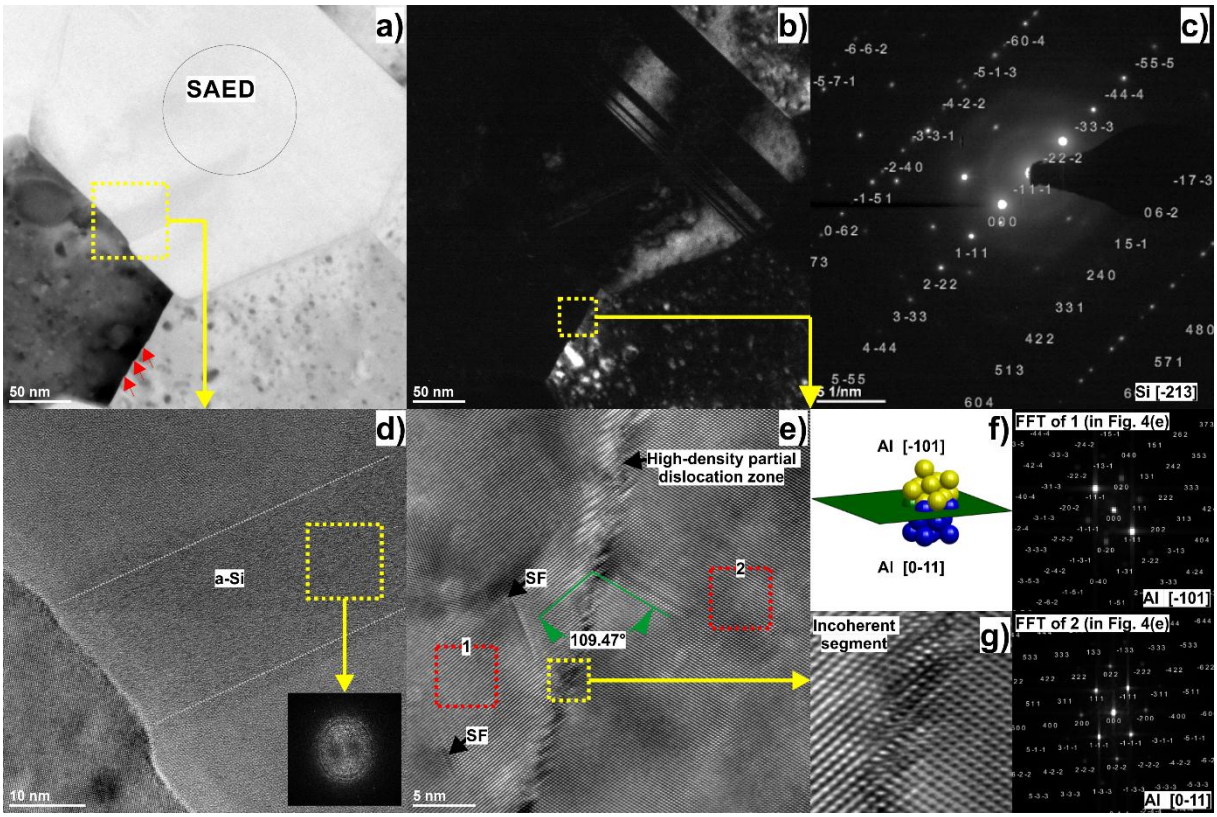

Figure 4. Representative TEM images of the KoBo sample a) bright field TEM image, b) dark- field TEM image – Both micrographs reveal a twinned Si precipitate with sharp boundaries. Note that the originally straight CTB has formed several kinks. These are highlighted by the red arrows in (a), c) SAED taken from the region highlighted in (a), d) HRTEM image of the heterophase boundary region highlighted in (a), e) HRTEM image of the boundary region highlighted in (b), (f) simulated atomic arrangement of the boundary region shown in (e), and (g) magnified view of the area highlighted by a yellow dashed square in (e) showing an incoherent segment within the CSL boundary.

Tensile tests were conducted at room temperature to assess the mechanical properties. Figure 5(a) displays the engineering stress-strain curves for two studied conditions. An analysis of the flow characteristics of both the as-built and KoBo-processed samples reveals that the KoBo-processed material exhibits a unique balance of strength and ductility, unlike the conventional trade-off. In other words, the KoBo-processed material shows moderate strength and excellent ductility compared to the as-built material. Additionally, as depicted in Figure 5, the KoBo-processed sample exhibits a yield phenomenon (upper yield point), as also observed by Avateffazeli et al. [73] in their study of the tensile properties of cast and SLM Al–Cu–Mg–Ag–TiB2 samples.

Figure 5(b) presents the work hardening rate versus true strain curves for the as-built and KoBo-processed conditions. Notably, the as-built sample displays a significantly higher work hardening rate compared to the KoBo-processed sample. This disparity can be attributed to a unique cellular structure that restricts the movement of dislocations around eutectic Si, contributing to the high work hardening rate [74] [75]. It's also worth mentioning that the failure of the as-built sample occurs at a work hardening rate of approximately 2000 MPa, which may be attributed to the presence of pore defects in the

PBF-LB/M part. The collapse of the initial cellular microstructure during KoBo extrusion results in a sharp reduction in the work hardening rate. Furthermore, the failure occurs at a minimal work hardening rate, indicating that the pore defects in the as-built sample were closed during the KoBo extrusion process.

Referencing to table 4, the as-built specimen exhibits a tensile strength of 422 MPa, a yield strength of 255 MPa, and an elongation of 2.4%. The KoBo specimen exhibits lower tensile strength of 324 MPa and yield strength of 185 MPa but much higher elongation break of about 10%, which proves to be a desirable property for subsequent post-processing steps.

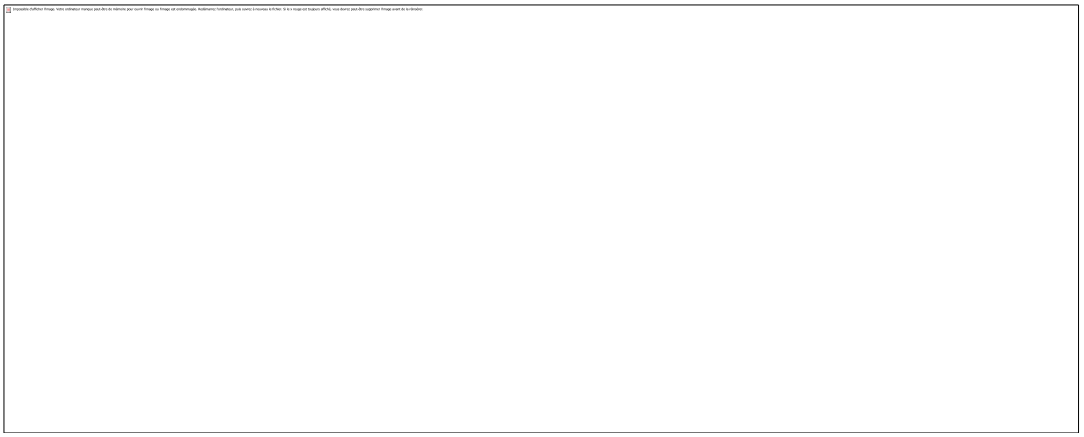

Figure 5. Experimental results from the tensile tests a) the representative engineering stress vs. engineering strain curves of as-built and KoBo processed samples, b) work hardening rate vs. true strain curves of as-built and KoBo processed samples

Table 4. Mechanical properties of the tested specimens

Condition	TS, MPa	YS, MPa	Elongation, %
As-built	422±4	255±3	2.4±0.1
KoBo	324±2	185±3	10.2±0.2

Figure 6 shows the fracture morphologies of as-built and KoBo-processed samples. As can be seen in Fig. 6(a) the as-built sample fractured at around 68° with respect to the tensile direction. The SEM images in Figs. 6(c) and (e), reveal a stepped cleavage surfaces (indicated by white arrows) typical for brittle fracture morphology, which is consistent with the low ductility shown in Fig. 5. The investigation displays that the fracture of KoBo-processed specimen occurred along the shear plane that around 51° with respect to the tensile axis. The SEM images in Figs. 6(d) and (f), reveal many fine dimples confirming a ductile fracture mode and good ductility shown in Fig. 5.

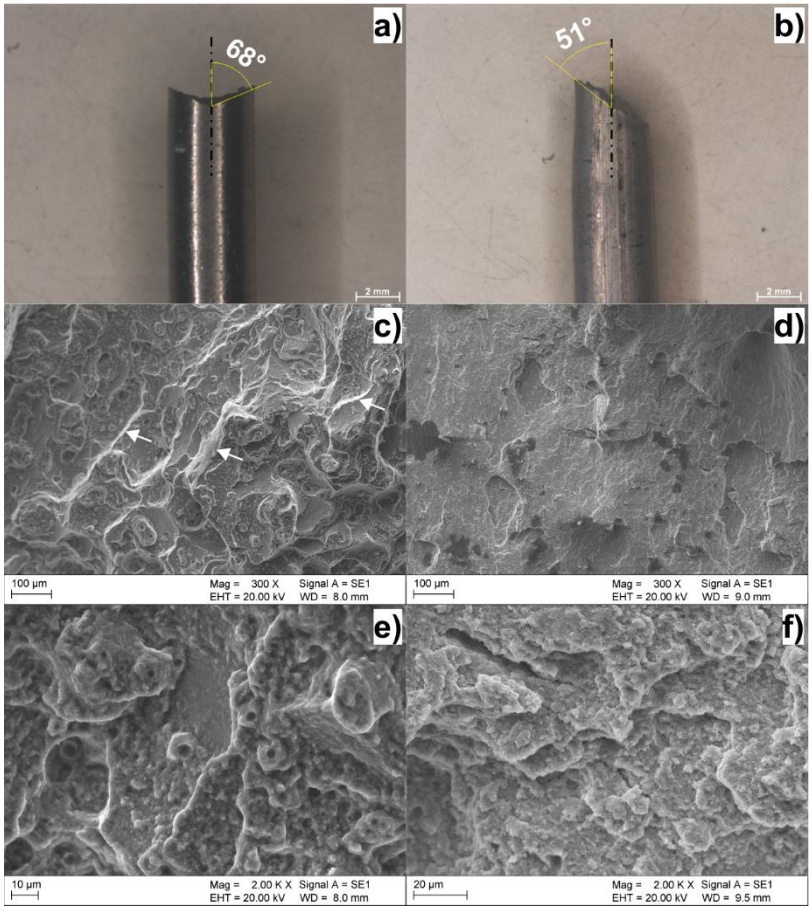

Figure 6. Fracture morphologies of the a), c) and e) as-built, b), d) and e) KoBo processed samples

Discussion

The KoBo extrusion process applied to the PBF-LB/M AlSi10Mg alloy resulted in remarkable changes in the microstructure, including grain size, phase morphology, distribution, and dislocation density. However, despite these changes, KoBo extrusion did not improve the mechanical properties of the PBF-LB/M alloy. In particular, the KoBo process impaired ductility, which is a commonly observed phenomenon [76]. The registered reduction in tensile strength can be attributed to the following main factors: a reduction in dislocation density (TEM and EBSD analyzes revealed nearly DRX dislocation-free grains) and the complete breakdown of the unique cellular network found in the PBF-LB/M alloy, as well as the coarsening of precipitates. From the present microstructural analysis, it is clear that the as-built sample has a cellular microstructure characterized by intricate dislocation networks that contribute greatly to its strength. These subcells in PBF-LB/M- Al-Si alloys are superstaurated with Si element. In the as-built condition, the Si content is typically above 10-11% (see Supplementary Figure S4); whereas, in the extruded KoBo sample, the Si content in an aluminium matrix is much lower, ranging between 6 and 9% (see Supplementary Figure S5). As a result, the effect of solid solution strengthening is also weaker.

The superior elongation of KoBo-processed sample can be caused by several factors. Firstly, it can be ascribed to the softening caused by recovery processes such as dynamic recrystallization [77]. As shown in supplementary Fig. S1, the DRX lead to the formation of the ultra-fine-grained microstructure characterized by a reduced dislocation density. During tensile testing, this fine-grained microstructure allows for a more gradual and distributed deformation across the specimen. Moreover, smaller grains are less prone to crack initiation and propagation, reducing the likelihood of premature failure [78]. Furthermore, the “dislocation-free” grains (Figs. 3(a) and 4(a)) promote a more even distribution of strain throughout the material during tensile test, inhibiting localized strain concentration, thus delaying the eventual fracture. A second factor influencing ductility is the increased fraction of stacking faults (SFs). Research has demonstrated that SFs can

alleviate stress concentration, leading to an enhancement in the proportional limit [29]. Moreover, the substantial presence of stacking faults in the aluminum matrix may also contribute to improved ductility by promoting mechanical twinning [11]. In addition to stacking faults, another noteworthy microstructural characteristic related to twinning was observed in this study using Electron Backscatter Diffraction (EBSD). This involves an exceptionally high percentage of low Σ-coincidence site lattice (CSL) boundaries. It has been demonstrated that the synergy between strength and ductility can be heightened by a high proportion of pre-existing annealing/deformation twins. This is because dislocations can easily glide and accumulate along the twin boundaries [79]. Therefore, the presence of twin boundaries / SFs does not result in a loss of ductility, as is often the case with traditional strengthening mechanisms [80].

Conclusions

In summary, we successfully post-processed a PBF-LB/M AlSi10Mg alloy using the KoBo extrusion process. The resulting alloy microstructure consists of an ultrafine-grained (UFG) (d∼0.81 μm) f.c.c. matrix with a high density of stacking faults, Σ-CSL boundaries. The main findings from this research can be summarized as follows:

- KoBo extrusion process with an extrusion ratio of 225 induces significant changes in the morphology of Si phase in the PBF-LB/M AlSi10Mg alloy. Microstructural investigation reveals unique cellular structure fragmentation and globularization.
- The KoBo process leads to a significant grain reduction in the grain size of the PBF-LB/M AlSi10Mg alloy. The experimental data revealed a grain size decrease from ~2.6 μm to ~0.8 μm.
- The KoBo process induces a high density of stacking faults and CSL twin boundaries in the aluminium matrix.
- The KoBo processed sample exhibits an attractive combination of mechanical properties (YS∼185 MPa, TS∼324MPa, E∼10.2%).

It is expected that such a unique microstructure might exhibit superior properties, i.e. improved radiation resistance (due to the higher intrinsic GB densities, which are sinks for radiation-induced defects), improved stability at high temperatures (the thermal stability of a coherent twin boundary is superior to that of a high-angle grain boundary), resistance to intergranular corrosion (a higher population of grain boundaries with low Σ-coincidence site lattice (CSL) can improve intergranular corrosion), and cyclic deformation (TBs have also been shown to be more resistant to cracking under cyclic loading). In essence, the results presented above confirm that it is possible to form ultrafine-grained nanotwinned microstructures in high SFE Al-Si alloy subjected to a high deformation rate (KoBo process).

Declaration of Competing Interest

The authors declare that they have no known competing financial interests or personal relationships that could have appeared to influence the work reported in this paper.

Funding

The research was funded by the National Science Centre, Poland based on the decision number 2021/43/D/ST8/01946.

This research was completed in association with the project Innovative and additive manufacturing technology—new technological solutions for 3D printing of metals and composite materials, reg. no. 319 CZ.02.1.01/0.0/0.0/17_049/0008407, financed by Structural Funds of the European Union.

References

[1] G. Li, Y. Yang, B. Gou, J. Zhang, J. Li, Y. Wang, L. Cao, G. Liu, X. Ding, J. Sun, Stabilizing defective coherent twin boundaries for strong and stable nanocrystalline nanotwinned Cu, Acta Mater. 241 (2022) 118368. https://doi.org/https://doi.org/10.1016/j.actamat.2022.118368.

[2] F. Jia, K.X. Wei, W. Wei, Q.B. Du, I. V Alexandrov, J. Hu, Effect of Sodium Dodecyl Sulfate on Mechanical Properties and Electrical Conductivity of Nanotwinned Copper, J. Mater. Eng. Perform. 29 (2020) 897–904. https://doi.org/10.1007/s11665-020-04674-4.

[3] K. Joshi, S.P. Joshi, On the micromechanics of voids in nanotwinned materials, J. Mech. Phys. Solids. 165 (2022) 104887. https://doi.org/https://doi.org/10.1016/j.jmps.2022.104887.

[4] Z. Shang, T. Niu, T. Sun, S. Xue, C. Fan, W.-Y. Chen, M. Li, H. Wang, X. Zhang, In situ study on radiation response of a nanotwinned steel, Scr. Mater. 220 (2022) 114920. https://doi.org/https://doi.org/10.1016/j.scriptamat.2022.114920.

[5] Z. Cheng, L. Bu, Y. Zhang, H. Wu, T. Zhu, L. Lu, Characterization of gradient plastic deformation in gradient nanotwinned Cu, Acta Mater. 246 (2023) 118673. https://doi.org/https://doi.org/10.1016/j.actamat.2023.118673.

[6] T. Wan, Z. Cheng, L. Bu, L. Lu, Work hardening discrepancy designing to strengthening gradient nanotwinned Cu, Scr. Mater. 201 (2021) 113975. https://doi.org/https://doi.org/10.1016/j.scriptamat.2021.113975.

[7] L.-P. Chang, J.-J. Wang, T.-H. Hung, K.-N. Chen, F.-Y. Ouyang, Direct metal bonding using nanotwinned Ag films with (111) surface orientation under air atmosphere for heterogeneous integration, Appl. Surf. Sci. 576 (2022) 151845. https://doi.org/https://doi.org/10.1016/j.apsusc.2021.151845.

[8] Y. Zhu, X. Hu, Y. Ni, Molecular dynamics simulation of microstructure evolution during the fracture process of nano-twinned Ag, Eng. Fract. Mech. 248 (2021) 107743. https://doi.org/https://doi.org/10.1016/j.engfracmech.2021.107743.

[9] Q. Li, D.Y. Liu, F.K. Yan, N.R. Tao, Martensitic transformation within nanotwins enhances fatigue damage resistance of a nanotwinned austenitic stainless steel, Scr. Mater. 207 (2022) 114313. https://doi.org/https://doi.org/10.1016/j.scriptamat.2021.114313.

[10] Y.Z. Zhang, J.J. Wang, N.R. Tao, Tensile ductility and deformation mechanisms of a nanotwinned 316L austenitic stainless steel, J. Mater. Sci. Technol. 36 (2020) 65–69. https://doi.org/https://doi.org/10.1016/j.jmst.2019.02.008.

[11] T. Jing, S. Dong, L. Shen, H. Peng, Y. Wen, Achieving strength-ductility synergy in nanotwinned steels prepared by cryogenic deformation, Mater. Charact. 195 (2023) 112512. https://doi.org/https://doi.org/10.1016/j.matchar.2022.112512.

[12] Y. Zhang, W.Q. Jiang, A. Gokhman, J.J. Yang, K. Shi, J.H. Luan, Y. Cui, P.K. Liaw, C.T. Liu, Z.W. Zhang, Enhanced irradiation tolerance of Fe30Cr25Ni20Co15Mn10 high-entropy alloy via nanotwin boundaries, J. Nucl. Mater. 557 (2021) 153292. https://doi.org/https://doi.org/10.1016/j.jnucmat.2021.153292.

[13] I. Lobzenko, D. Wei, M. Itakura, Y. Shiihara, T. Tsuru, Improved mechanical properties of Co-free high-entropy Cantor alloy: A first-principles study, Results Mater. 17 (2023) 100364. https://doi.org/https://doi.org/10.1016/j.rinma.2023.100364.

[14] L. Lu, X. Chen, X. Huang, K. Lu, Revealing the Maximum Strength in Nanotwinned Copper, Science (80-.). 323 (2009) 607–610. https://doi.org/10.1126/science.1167641.

[15] O. Anderoglu, A. Misra, H. Wang, F. Ronning, M.F. Hundley, X. Zhang, Epitaxial nanotwinned Cu films with high strength and high conductivity, Appl. Phys. Lett. 93 (2008) 83108. https://doi.org/10.1063/1.2969409.

[16] J. Sun, Q. Li, H. Tang, H. Zhang, H. Ye, Y. Zheng, Helium implantation effects on the tensile response of nano-twinned copper, J. Nucl. Mater. 541 (2020) 152426. https://doi.org/https://doi.org/10.1016/j.jnucmat.2020.152426.

[17] C. Fan, D. Xie, J. Li, Z. Shang, Y. Chen, S. Xue, J. Wang, M. Li, A. El-Azab, H. Wang, X. Zhang, 9R phase enabled superior radiation stability of nanotwinned Cu alloys via in situ radiation at elevated temperature, Acta Mater. 167 (2019) 248–256. https://doi.org/https://doi.org/10.1016/j.actamat.2019.01.037.

[18] H.H. Chen, Y.F. Zhao, J.Y. Zhang, Y.Q. Wang, G.Y. Li, K. Wu, G. Liu, J. Sun, He-ion irradiation effects on the microstructure stability and size-dependent mechanical behavior of high entropy alloy/Cu nanotwinned nanolaminates, Int. J. Plast. 133 (2020) 102839. https://doi.org/https://doi.org/10.1016/j.ijplas.2020.102839.

[19] Y. Yu, Y. Yu, Simulations of irradiation resistance and mechanical properties under irradiation of high-entropy alloy NiCoCrFe, Mater. Today Commun. 33 (2022) 104308. https://doi.org/https://doi.org/10.1016/j.mtcomm.2022.104308.

[20] J. Tang, C. Xu, Z. Li, X. Tian, W. Jiang, Q. Wang, H. Fan, Interaction between <c> dislocation loop and {101¯2} twin boundary in magnesium, J. Nucl. Mater. 560 (2022) 153495. https://doi.org/https://doi.org/10.1016/j.jnucmat.2021.153495.

[21] T. Niu, J. Li, Y. Zhang, J. Cho, J. Ding, R. Su, S. Xue, C. Fan, Z. Shang, D. Chen, Y. Wang, H. Wang, X. Zhang, In-situ studies on the mechanical properties of He ion irradiated nanotwinned Ag, J. Nucl. Mater. 540 (2020) 152392. https://doi.org/https://doi.org/10.1016/j.jnucmat.2020.152392.

[22] T. Ma, H. Kim, N. Mathew, D.J. Luscher, L. Cao, A. Hunter, Dislocation transmission across Σ3{112} incoherent twin boundary: a combined atomistic and phase-field study, Acta Mater. 223 (2022) 117447. https://doi.org/https://doi.org/10.1016/j.actamat.2021.117447.

[23] D. Bhattacharyya, X.-Y. Liu, A. Genc, H.L. Fraser, R.G. Hoagland, A. Misra, Heterotwin formation during growth of nanolayered Al-TiN composites, Appl. Phys. Lett. 96 (2010) 93113. https://doi.org/10.1063/1.3330889.

[24] N.A. Richter, M. Gong, Y.F. Zhang, T. Niu, B. Yang, J. Wang, H. Wang, X. Zhang, Exploring the deformation behavior of nanotwinned Al–Zr alloy via in situ compression, J. Appl. Phys. 132 (2022) 65104. https://doi.org/10.1063/5.0098497.

[25] N.A. Richter, Y.F. Zhang, D.Y. Xie, R. Su, Q. Li, S. Xue, T. Niu, J. Wang, H. Wang, X. Zhang, Microstructural evolution of nanotwinned Al-Zr alloy with significant 9R phase, Mater. Res. Lett. 9 (2021) 91–98. https://doi.org/10.1080/21663831.2020.1840451.

[26] M. Liu, P. Wang, G. Lu, C.-Y. Huang, Z. You, C.-H. Wang, H.-W. Yen, Deformation-activated recrystallization twin: New twinning path in pure aluminum enabled by cryogenic and rapid compression, IScience. 25 (2022) 104248. https://doi.org/https://doi.org/10.1016/j.isci.2022.104248.

[27] B. Guo, M. Song, X. Zhang, Y. Liu, X. Cen, B. Chen, W. Li, Exploiting the synergic strengthening effects of stacking faults in carbon nanotubes reinforced aluminum matrix composites for enhanced mechanical properties, Compos. Part B Eng. 211 (2021) 108646. https://doi.org/https://doi.org/10.1016/j.compositesb.2021.108646.

[28] D. Gong, Y. Cao, X. Deng, L. Jiang, Higher proportional limit of SiC/Al composites with nano-scaled stacking faults, Compos. Commun. 32 (2022) 101188. https://doi.org/https://doi.org/10.1016/j.coco.2022.101188.

[29] D. Gong, M. Zhu, Z. You, H. Han, Z. Chao, L. Jiang, In-situ TEM study on the effect of stacking faults on micro-plasticity and proportional limit in SiC/Al composites, Compos. Part B Eng. 244 (2022) 110180. https://doi.org/https://doi.org/10.1016/j.compositesb.2022.110180.

[30] X.Z. Liao, S.G. Srinivasan, Y.H. Zhao, M.I. Baskes, Y.T. Zhu, F. Zhou, E.J. Lavernia, H.F. Xu, Formation mechanism of wide stacking faults in nanocrystalline Al, Appl. Phys. Lett. 84 (2004) 3564–3566. https://doi.org/10.1063/1.1734689.

[31] S. Xue, Z. Fan, O.B. Lawal, R. Thevamaran, Q. Li, Y. Liu, K.Y. Yu, J. Wang, E.L. Thomas, H. Wang, X. Zhang, High-velocity projectile impact induced 9R phase in ultrafine-grained aluminium, Nat. Commun. 8 (2017) 1653. https://doi.org/10.1038/s41467-017-01729-4.

[32] Q. Xiong, Z. Li, X. Huang, T. Shimada, T. Kitamura, Thermomechanical conversion in high-rate plastic deformation of nanotwinned polycrystalline copper, J. Therm. Stress. 45 (2022) 65–80.

https://doi.org/10.1080/01495739.2021.2000343.

[33] A.A. Tiamiyu, E.L. Pang, X. Chen, J.M. LeBeau, K.A. Nelson, C.A. Schuh, Nanotwinning-assisted dynamic recrystallization at high strains and strain rates, Nat. Mater. 21 (2022) 786–794. https://doi.org/10.1038/s41563-022-01250-0.

[34] Y.L. Bian, Z.D. Feng, N.B. Zhang, Y.X. Li, X.F. Wang, B.B. Zhang, Y. Cai, L. Lu, S. Chen, X.H. Yao, S.N. Luo, Ultrafast severe plastic deformation in high-entropy alloy Al0.1CoCrFeNi via dynamic equal channel angular pressing, Mater. Sci. Eng. A. 847 (2022) 143221. https://doi.org/https://doi.org/10.1016/j.msea.2022.143221.

[35] R.Z. Valiev, T.G. Langdon, Principles of equal-channel angular pressing as a processing tool for grain refinement, Prog. Mater. Sci. 51 (2006) 881–981. https://doi.org/10.1016/j.pmatsci.2006.02.003.

[36] A.P. Zhilyaev, T.G. Langdon, Using high-pressure torsion for metal processing: Fundamentals and applications, Prog. Mater. Sci. (2008). https://doi.org/10.1016/j.pmatsci.2008.03.002.

[37] N. Tsuji, Y. Saito, S.-H. Lee, Y. Minamino, ARB (Accumulative Roll-Bonding) and other new Techniques to Produce Bulk Ultrafine Grained Materials, Adv. Eng. Mater. 5 (2003) 338–344. https://doi.org/https://doi.org/10.1002/adem.200310077.

[38] S.B. Jin, K. Zhang, R. Bjørge, N.R. Tao, K. Marthinsen, K. Lu, Y.J. Li, Formation of incoherent deformation twin boundaries in a coarse-grained Al-7Mg alloy, Appl. Phys. Lett. 107 (2015) 91901. https://doi.org/10.1063/1.4929683.

[39] A. Korbel, L. Błaż, W. Bochniak, M. Pawlyta, P. Ostachowski, M. Łagoda, Nano-Dimensional Elements in the Structure of Zinc Subjected to KOBO Extrusion, Metallogr. Microstruct. Anal. (2023). https://doi.org/10.1007/s13632-023-00945-3.

[40] C. Dai, P. Saidi, Z. Yao, L.K. Béland, M.R. Daymond, Deformation-free nanotwin formation in zirconium and titanium, Mater. Lett. 247 (2019) 111–114. https://doi.org/https://doi.org/10.1016/j.matlet.2019.03.029.

[41] E. Maleki, S. Bagherifard, O. Unal, M. Bandini, M. Guagliano, The effects of microstructural and chemical surface gradients on fatigue performance of laser powder bed fusion AlSi10Mg, Mater. Sci. Eng. A. 840 (2022) 142962. https://doi.org/https://doi.org/10.1016/j.msea.2022.142962.

[42] E. Maleki, S. Bagherifard, A. Heydari Astaraee, S. Sgarbazzini, M. Bandini, M. Guagliano, Application of gradient severe shot peening as a novel mechanical surface treatment on fatigue behavior of additively manufactured AlSi10Mg, Mater. Sci. Eng. A. 881 (2023) 145397. https://doi.org/https://doi.org/10.1016/j.msea.2023.145397.

[43] E. Maleki, S. Bagherifard, N. Razavi, M. Riccio, M. Bandini, A. du Plessis, F. Berto, M. Guagliano, Fatigue behaviour of notched laser powder bed fusion AlSi10Mg after thermal and mechanical surface post-processing, Mater. Sci. Eng. A. 829 (2022) 142145. https://doi.org/https://doi.org/10.1016/j.msea.2021.142145.

[44] F. Alghamdi, X. Song, A. Hadadzadeh, B. Shalchi-Amirkhiz, M. Mohammadi, M. Haghshenas, Post heat treatment of additive manufactured AlSi10Mg: On silicon morphology, texture and small-scale properties, Mater. Sci. Eng. A. 783 (2020) 139296. https://doi.org/https://doi.org/10.1016/j.msea.2020.139296.

[45] F. Alghamdi, M. Haghshenas, Microstructural and small-scale characterization of additive manufactured AlSi10Mg alloy, SN Appl. Sci. 1 (2019) 255. https://doi.org/10.1007/s42452-019-0270-5.

[46] S.I. Shakil, A. Hadadzadeh, B. Shalchi Amirkhiz, H. Pirgazi, M. Mohammadi, M. Haghshenas, Additive manufactured versus cast AlSi10Mg alloy: Microstructure and micromechanics, Results Mater. 10 (2021) 100178. https://doi.org/https://doi.org/10.1016/j.rinma.2021.100178.

[47] A. Hosseinzadeh, A. Radi, J. Richter, T. Wegener, S.V. Sajadifar, T. Niendorf, G.G. Yapici, Severe plastic deformation as a processing tool for strengthening of additive manufactured alloys, J. Manuf. Process. 68 (2021) 788–795. https://doi.org/https://doi.org/10.1016/j.jmapro.2021.05.070.

[48] A. Heidarzadeh, M. Javidani, M. Mofarrehi, P. Motalleb-nejad, R. Mohammadzadeh, H. Jafarian, X.-G. Chen, Grain Structure Formation and Texture Modification through Multi-Pass Friction Stir Processing in AlSi10Mg Alloy Produced by Laser Powder Bed Fusion, Materials (Basel). 16 (2023). https://doi.org/10.3390/ma16030944.

[49] W. Feng, Z. Wang, Q. Sun, Y. He, Y. Sun, Effect of thermomechanical processing via rotary swaging on grain boundary character distribution and intergranular corrosion in 304 austenitic stainless steel, J. Mater. Res. Technol. 19 (2022) 2470–2482. https://doi.org/https://doi.org/10.1016/j.jmrt.2022.06.032.

[50] T.-F. Chung, S.-Y. Lu, Y.-S. Lin, Y.-L. Li, P.-H. Chiu, C.-N. Hsiao, C.-Y. Chen, C.-L. Kuo, J.-W. Yeh, S.-H. Wang, W.-S. Lee, J.-R. Yang, Hierarchical nanotwins in Fe27Co24Ni23Cr26 high-entropy alloy subjected to high strain-rate Hopkinson bar deformation, Mater. Charact. 185 (2022) 111737. https://doi.org/https://doi.org/10.1016/j.matchar.2022.111737.

[51] L. Qian, Z. Cui, C. Sun, S. Geng, Z. Sun, Investigation of deformation compatibility and power consumption during KOBO extrusion of bimetallic composite tube, Int. J. Adv. Manuf. Technol. 118 (2022) 3477–3486. https://doi.org/10.1007/s00170-021-08608-9.

[52] W. Bochniak, K. Marszowski, A. Korbel, Theoretical and practical aspects of the production of thin-walled tubes by the KOBO method, J. Mater. Process. Technol. 169 (2005) 44–53. https://doi.org/https://doi.org/10.1016/j.jmatprotec.2005.02.258.

[53] A. Nittala, J. Smith, B. Gwalani, J. Silverstein, F.F. Kraft, K. Kappagantula, Simultaneously improved electrical and mechanical performance of hot-extruded bulk scale aluminum-graphene wires, Mater. Sci. Eng. B. 293 (2023) 116452. https://doi.org/https://doi.org/10.1016/j.mseb.2023.116452.

[54] P. Koprowski, M. Lech-Grega, Ł. Wodziński, B. Augustyn, S. Boczkal, M. Ożóg, P. Uliasz, J. Żelechowski, W. Szymański, The effect of low content additives on strength, resistivity and microstructural changes in wire drawing of 1xxx series aluminium alloys for electrical purposes, Mater. Today Commun. 24 (2020) 101039. https://doi.org/https://doi.org/10.1016/j.mtcomm.2020.101039.

[55] L. Cabrera-Correa, L. González-Rovira, J. de Dios López-Castro, M. Castillo-Rodríguez, F.J. Botana, Effect of the heat treatment on the mechanical properties and microstructure of Scalmalloy® manufactured by Selective Laser Melting (SLM) under certified conditions, Mater. Charact. 196 (2023) 112549. https://doi.org/https://doi.org/10.1016/j.matchar.2022.112549.

[56] B. Dong, X. Cai, F. Chen, S. Lin, Y. Zong, D. Shan, Twinned dendrites growth in wire arc directed energy deposition of Al-Zn-Mg-Cu alloy, Mater. Des. 228 (2023) 111821. https://doi.org/https://doi.org/10.1016/j.matdes.2023.111821.

[57] S. V Danilov, P.L. Reznik, M.A. Zorina, M.L. Lobanov, Effect of special boundaries on recrystallization texture of FCC metals with high packing defect energy, AIP Conf. Proc. 2174 (2019) 20207. https://doi.org/10.1063/1.5134358.

[58] S. Pradeep, V.K.S. Jain, S. Muthukumaran, R. Kumar, Microstructure and texture evolution during multi-pass friction stir processed AA5083, Mater. Lett. 288 (2021) 129382. https://doi.org/https://doi.org/10.1016/j.matlet.2021.129382.

[59] R. Li, E.R. Homer, C. Hong, Y. Zhang, D.J. Jensen, An experimentally-based molecular dynamics analysis of grain boundary migration during recrystallization in aluminum, Scr. Mater. 211 (2022) 114489. https://doi.org/https://doi.org/10.1016/j.scriptamat.2021.114489.

[60] Q. Tan, J. Zhang, N. Mo, Z. Fan, Y. Yin, M. Bermingham, Y. Liu, H. Huang, M.X. Zhang, A novel method to 3D-print fine-grained AlSi10Mg alloy with isotropic properties via inoculation with LaB6 nanoparticles, Addit. Manuf. 32 (2020) 101034. https://doi.org/10.1016/J.ADDMA.2019.101034.

[61] W. Lefebvre, G. Rose, P. Delroisse, E. Baustert, F. Cuvilly, A. Simar, Nanoscale periodic gradients generated by laser

powder bed fusion of an AlSi10Mg alloy, Mater. Des. 197 (2021) 109264. https://doi.org/https://doi.org/10.1016/j.matdes.2020.109264.

[62] P. Snopiński, O. Hilšer, J. Hajnyš, Tuning the defects density in additively manufactured fcc aluminium alloy via modifying the cellular structure and post-processing deformation, Mater. Sci. Eng. A. 865 (2023) 144605. https://doi.org/https://doi.org/10.1016/j.msea.2023.144605.

[63] D.G. Brandon, The structure of high-angle grain boundaries, Acta Metall. 14 (1966) 1479–1484. https://doi.org/https://doi.org/10.1016/0001-6160(66)90168-4.

[64] L. Wang, J. Teng, Y. Wu, X. Sha, S. Xiang, S. Mao, G. Yu, Z. Zhang, J. Zou, X. Han, In situ atomic scale mechanisms of strain-induced twin boundary shear to high angle grain boundary in nanocrystalline Pt, Ultramicroscopy. 195 (2018) 69–73. https://doi.org/https://doi.org/10.1016/j.ultramic.2018.08.022.

[65] D. Bufford, Y. Liu, Y. Zhu, Z. Bi, Q.X. Jia, H. Wang, X. Zhang, Formation Mechanisms of High-density Growth Twins in Aluminum with High Stacking-Fault Energy, Mater. Res. Lett. 1 (2013) 51–60. https://doi.org/10.1080/21663831.2012.761654.

[66] C. Cayron, Reply to “Response to “Diffraction artefacts from twins and stacking faults, and the mirage of hexagonal, polytypes or other superstructures"”, Scr. Mater. 203 (2021) 114115. https://doi.org/https://doi.org/10.1016/j.scriptamat.2021.114115.

[67] J.D. Zuo, C. He, M. Cheng, K. Wu, Y.Q. Wang, J.Y. Zhang, G. Liu, J. Sun, Heterophase interface-mediated formation of nanotwins and 9R phase in aluminum: Underlying mechanisms and strengthening effect, Acta Mater. 174 (2019) 279–288. https://doi.org/https://doi.org/10.1016/j.actamat.2019.05.053.

[68] J. Zhang, D. Zhou, X. Pang, B. Zhang, Y. Li, B. Sun, R.Z. Valiev, D. Zhang, Deformation-induced concurrent formation of 9R phase and twins in a nanograined aluminum alloy, Acta Mater. 244 (2023) 118540. https://doi.org/https://doi.org/10.1016/j.actamat.2022.118540.

[69] P. Snopiński, Exploring microstructure refinement and deformation mechanisms in severely deformed LPBF AlSi10Mg alloy, J. Alloys Compd. 941 (2023) 168984. https://doi.org/https://doi.org/10.1016/j.jallcom.2023.168984.

[70] Y. He, L. Zhong, F. Fan, C. Wang, T. Zhu, S.X. Mao, In situ observation of shear-driven amorphization in silicon crystals, Nat. Nanotechnol. 11 (2016) 866–871. https://doi.org/10.1038/nnano.2016.166.

[71] V. Yamakov, D. Wolf, S.R. Phillpot, A.K. Mukherjee, H. Gleiter, Dislocation processes in the deformation of nanocrystalline aluminium by molecular-dynamics simulation, Nat. Mater. 1 (2002) 45–49. https://doi.org/10.1038/nmat700.

[72] J.P. Hirth, R.G. Hoagland, Extrinsically dissociated dislocations in simulated aluminium, Philos. Mag. A. 78 (1998) 529–532. https://doi.org/10.1080/01418619808241920.

[73] M. Avateffazeli, P.E. Carrion, B. Shachi-Amirkhiz, H. Pirgazi, M. Mohammadi, N. Shamsaei, M. Haghshenas, Correlation between tensile properties, microstructure, and processing routes of an Al–Cu–Mg–Ag–TiB2 (A205) alloy: Additive manufacturing and casting, Mater. Sci. Eng. A. 841 (2022) 142989. https://doi.org/https://doi.org/10.1016/j.msea.2022.142989.

[74] Z. Li, Z. Li, Z. Tan, D.B. Xiong, Q. Guo, Stress relaxation and the cellular structure-dependence of plastic deformation in additively manufactured AlSi10Mg alloys, Int. J. Plast. (2020). https://doi.org/10.1016/j.ijplas.2019.12.003.

[75] B. Chen, S.K. Moon, X. Yao, G. Bi, J. Shen, J. Umeda, K. Kondoh, Strength and strain hardening of a selective laser melted AlSi10Mg alloy, Scr. Mater. (2017). https://doi.org/10.1016/j.scriptamat.2017.07.025.

[76] A. Dobkowska, A. Zielińska, I. Paulin, Č. Donik, M. Łojkowski, M. Koralnik, B. Adamczyk-Cieślak, K. Paradowski, M. Tkocz, D. Kuc, J. Kubásek, M. Godec, W. Święszkowski, Microstructure and properties of an AZ61 alloy after

extrusion with a forward-backward oscillating die without preheating of the initial billet, J. Alloys Compd. 952 (2023) 169843. https://doi.org/https://doi.org/10.1016/j.jallcom.2023.169843.

[77] D. Garbiec, V. Leshchynsky, A. García-Junceda, R. Swadźba, P. Siwak, G. Adamek, K. Radwański, Microstructure and Mechanical Properties of Spark Plasma Sintered and Severely Deformed AA7075 Alloy, Metals (Basel). 11 (2021). https://doi.org/10.3390/met11091433.

[78] B. Bagheri, M. Alizadeh, S.E. Mirsalehi, A. Shamsipur, A. Abdollahzadeh, Nanoparticles Addition in AA2024 Aluminum/Pure Copper Plate: FSSW Approach, Microstructure Evolution, Texture Study, and Mechanical Properties, JOM. 74 (2022) 4420–4433. https://doi.org/10.1007/s11837-022-05481-z.

[79] M. Huang, P. Zhai, S.I. Morozov, W.A. Goddard, G. Li, Q. Zhang, Engineering twin boundaries for enhancing strength and ductility of thermoelectric semiconductor PbTe, J. Alloys Compd. 959 (2023) 170429. https://doi.org/https://doi.org/10.1016/j.jallcom.2023.170429.

[80] S. Taali, M.R. Toroghinejad, M. Kuglstatter, H.W. Höppel, Grain boundary engineering in roll-bonded copper to overcome the strength-ductility dilemma, J. Mater. Res. Technol. 17 (2022) 3198–3204. https://doi.org/https://doi.org/10.1016/j.jmrt.2022.02.032.